

Space–Time Correlations in Two Subsonic Jets Using Dual Particle Image Velocimetry Measurements

Vincent Fleury*

ONERA, 92322 Châtillon, France

and

Christophe Bailly,[†] Emmanuel Jondeau,[‡] Marc Michard,[§] and Daniel Juve[¶]

Ecole Centrale de Lyon, 69134 Ecully, France

DOI: 10.2514/1.35561

Dual particle image velocimetry (dual PIV) measurements have been performed to investigate the space–time correlations in two subsonic isothermal round jets at Mach numbers of 0.6 and 0.9. The correlation scales are analyzed along the centerline and in the shear-layer center over the first 11 jet diameters from the nozzle exit. To provide robust results over a wide range of flow conditions, these correlation scales are given in terms of their appropriate quantities, namely, the mean or rms velocity in reference to velocity and the momentum thickness or the half-velocity diameter in reference to length in the shear layer and on the jet axis, respectively. From these results, a discussion on the modeling of turbulence in jets is addressed. The self-similarity of some space correlation functions in the shear layer and on the jet axis is shown. Furthermore, far enough downstream in the shear layer, some of the ratios between the space and time scales are relatively close to the values expected in homogeneous and isotropic turbulence. It is also found that the ratio between the integral length and the time scales in the fixed frame is of the order of the local mean flow velocity. In the convected frame, the appropriate scaling factor is the rms velocity.

Nomenclature

c_0	= ambient sound speed
D	= jet exit diameter
$D_{1/2}$	= half-velocity diameter, $U_1(x_1, x_2 = D_{1/2}/2) = U_a/2$
L_c	= potential core length, axial length where $U_a \geq 0.95 \times U_j$
L_{cii}	= length scale in the convected frame, $L_{cii} = U_c T_{cii}$
$L_{ii}^{(j)}$	= integral length scale
M	= jet Mach number, $U_1(x_1 = 0, x_2 = 0)/c_0$
M_c	= convection Mach number, U_c/c_0
$R_{ii}(\mathbf{x}, \boldsymbol{\xi}, \tau)$	= autocorrelation function
T_{cii}	= integral time scale in the convected frame
T_{ii}	= integral time scale in the fixed frame
t	= time
U_a	= mean velocity on the jet axis, $U_1(x_1, x_2 = 0)$
U_c	= convection velocity, $\ d\boldsymbol{\xi}_c/d\tau\ $

U_i	= mean velocity
u'_i	= velocity fluctuation
u_i	= root mean square value of u'_i , $u_i = \sqrt{\overline{u_i'^2}}$ where the overline operator stands for ensemble averaging
U_j	= jet exit velocity, $U_1(x_1 = 0, x_2 = 0)$
x_i, z_i	= positions; the origin is located at the center of the nozzle, in the exit plane
δ_θ	= momentum quantity
Θ_{cii}	= reference time for the convected frame, $L_{ii}^{(1)}/u_i$
Θ_{ii}	= reference time for the fixed frame, $L_{ii}^{(1)}/U_1$
ξ_{ci}	= location of the correlation peak in the convected frame
ξ_i	= separation vector in the fixed frame
$\xi_{0i}^{+(j)}, \xi_{0i}^{-(j)}$	= locations of first zero crossing of $R_{ii}(\mathbf{x}, \boldsymbol{\xi}_j, \tau = 0)$, where $\xi_{0i}^{+(j)} > 0$ and $\xi_{0i}^{-(j)} < 0$
τ	= time delay
τ_{0ii}	= time delay to first zero crossing of $R_{ii}(\mathbf{x}, \boldsymbol{\xi} = 0, \tau)$

Presented as Paper 3615 at the 13th AIAA/CEAS Aeroacoustics Conference (28th AIAA Aeroacoustics Conference), Rome, 21–23 May 2007; received 12 November 2007; revision received 10 June 2008; accepted for publication 18 June 2008. Copyright © 2008 by the authors. Published by the American Institute of Aeronautics and Astronautics, Inc., with permission. Copies of this paper may be made for personal or internal use, on condition that the copier pay the \$10.00 per-copy fee to the Copyright Clearance Center, Inc., 222 Rosewood Drive, Danvers, MA 01923; include the code 0001-1452/08 \$10.00 in correspondence with the CCC.

*Research Engineer, Département de Simulation Numérique et Aéroacoustique; vincent.fleury@onera.fr.

[†]Professor, Ecole Centrale de Lyon and Institut Universitaire de France, Laboratoire de Mécanique des Fluides et d'Acoustique, Unité Mixte de Recherche 5509 du Centre National de la Recherche Scientifique; christophe.bailly@ec-lyon.fr. Senior Member AIAA.

[‡]Engineer, Laboratoire de Mécanique des Fluides et d'Acoustique, Unité Mixte de Recherche 5509 du Centre National de la Recherche Scientifique; emmanuel.jondeau@ec-lyon.fr.

[§]Associate Professor, Institut National des Sciences Appliquées de Lyon and Laboratoire de Mécanique des Fluides et d'Acoustique, Unité Mixte de Recherche 5509 du Centre National de la Recherche Scientifique; marc.michard@ec-lyon.fr.

[¶]Professor, Laboratoire de Mécanique des Fluides et d'Acoustique, Unité Mixte de Recherche 5509 du Centre National de la Recherche Scientifique; daniel.juve@ec-lyon.fr. Senior Member AIAA.

Subscripts and Superscripts

1	= component in the axial direction
2	= component in the radial direction

I. Introduction

THE concept of correlation is well adapted to characterize the space–time statistical properties of turbulence. As an example, one of the first applications to aerodynamic noise was derived by Proudman [1] from the theory developed by Lighthill [2,3]. To estimate the acoustic intensity $I(\mathbf{z})$, Proudman introduced the correlations of the turbulent fluctuations and related this quantity to the fourth-order time derivative of the two-point two-time correlation of the Lighthill tensor. For isentropic, stationary, low Mach number and high Reynolds number flows, this reduces to

$$I(\mathbf{z}) = \frac{1}{16\pi^2 \rho_0 c_0^5 z^2} \times \frac{z_i z_j z_k z_l}{z^4} \iint \frac{\partial^4}{\partial \tau_a^4} \overline{(u'_i u'_j)_{\mathbf{x},t} (u'_k u'_l)_{\mathbf{x}+\boldsymbol{\xi},t+\tau_a}} \Big|_{\tau_a=\mathbf{z}\boldsymbol{\xi}/(c_0 z)} d\xi^3 dx^3$$

where τ_a is the retarded time. The problem then reduces to the evaluation of the integration of the fourth-order velocity correlations over the flow domain. Ribner [4] tackled this problem by considering isotropic turbulence superimposed on a mean shear axisymmetric flow. The derivation of the model is not reproduced, but through usual statistical assumptions, the integrand is expressed as a function of second-order velocity correlations. To develop an engineering tool, a reasonable idea is to first introduce some numerical data provided by a k - ϵ turbulence model. Béchara et al. [5], Bailly et al. [6], and Khavaran [7], among others, developed such applications to subsonic and supersonic jet noise. Note that a connected and interesting discussion has been proposed by Morris and Farassat [8]. Assuming a separation of variables, the space–time second-order velocity autocorrelation function

$$R_{ii}(\mathbf{x}, \boldsymbol{\xi}, \tau) = \frac{\overline{u'_i(\mathbf{x}, t)u'_i(\mathbf{x} + \boldsymbol{\xi}, t + \tau)}}{[u_i(\mathbf{x})u_i(\mathbf{x} + \boldsymbol{\xi})]^{-1}}$$

is usually expressed as

$$R_{ii}(\mathbf{x}, \boldsymbol{\xi}, \tau) = f\left[\left(\frac{\xi_j}{L_{ii}^{(j)}}\right)_{j=1\dots 3}\right]g\left[\frac{\tau}{T_{ii}}\right] \quad (1)$$

in the fixed frame, and

$$R_{ii}(\mathbf{x}, \mathbf{U}_c \tau + \boldsymbol{\xi}, \tau) = f\left[\left(\frac{\xi_j}{L_{ii}^{(j)}}\right)_{j=1\dots 3}\right]g\left[\frac{\tau}{T_{cii}}\right] \quad (2)$$

in the convected frame. Here,

$$L_{ii}^{(j)} = \frac{1}{2} \int_{\xi_{0i}^{-(j)}}^{\xi_{0i}^{+(j)}} R_{ii}(\mathbf{x}, \boldsymbol{\xi}, \tau = 0) d\xi_j$$

is an integral space scale and

$$T_{ii} = \int_0^{\tau_{0i}} R_{ii}(\mathbf{x}, \boldsymbol{\xi} = 0, \tau) d\tau$$

and

$$T_{cii} = \int_0^{\tau_{0i}} R_{ii}(\mathbf{x}, \boldsymbol{\xi} = \mathbf{U}_c \tau, \tau) d\tau$$

are integral time scales in the fixed frame and in the convected frame, respectively. The functions f and g and the space–time integral scales are taken from experiments or semi-empirical relations; for instance, see Ribner [9], Goldstein and Rosenbaum [10], or Morris and Farassat [8]. Note also that, with the progress of time-dependent Navier–Stokes simulations, a direct computation of these functions is also possible, as proposed by Morris et al. [11] and He et al. [12], for instance.

Several experiments have been devoted to the measurement of the correlation scales of velocity in nearly isotropic grid-generated turbulence [13]. A detailed bibliography of the pioneering investigations can be found in Comte-Bellot and Corrsin [14]. In such flows, the turbulence decreases due to viscous dissipation effects only. From physical arguments, Batchelor [15] and Townsend [16] estimated the space and time integral scales according to the viscous dissipation rate ϵ and u_1 as follows:

$$\epsilon \approx \alpha \frac{u_1^2}{L_{11}^{(1)}/u_1} \quad \text{or} \quad \epsilon \approx \alpha \frac{u_1^2}{\Theta_{c11}}$$

where the constant α is of the order of unity. This was confirmed experimentally by Comte-Bellot and Corrsin [17], who obtained a value of α close to 1. In a free shear flow, turbulence decay is mainly due to the intensity of the mean velocity gradients. The measurements of Davies et al. [18] supplied the following estimates

of the integral scales $L_{11}^{(1)}$ and T_{11} in the mixing-layer of a jet:

$$L_{11}^{(1)} \approx \frac{5u_1}{|dU_1/dx_2|} \quad \text{and} \quad T_{c11} \approx \frac{3}{|dU_1/dx_2|}$$

Assuming a hyperbolic tangent profile for the mean flow (see also Eq. (4) in Sec. III), the mean velocity gradient can be estimated by $|dU_1/dx_2| \approx U_J/(4\delta_\theta)$. By noting [18,19] that $u_1/U_J \approx 0.16$, the two following equivalent relations can then be derived:

$$L_{11}^{(1)} \approx 3.2\delta_\theta \quad \text{and} \quad T_{c11} \approx 12 \frac{\delta_\theta}{U_J} \approx 0.6\Theta_{c11} \quad (3)$$

The scaling of a characteristic time associated with the correlation function according to U_J and δ_θ is in agreement with the results found by Dimotakis and Brown [20] in a planar turbulent mixing layer. In these investigations, the velocity fluctuations have been measured with two single hot wires, and thus only the correlation of the axial velocity could be characterized. With the development of new measurement techniques, the database on velocity correlations in jets has filled out. Using laser Doppler anemometry (LDA), Lau [21] and Kerhervé et al. [22] investigated the correlation of the radial and axial velocity components in high-speed jets. More recently, the development of particle image velocimetry (PIV) has allowed the exploration of the correlation functions over a 2-D map and for a large, almost unlimited, number of reference points. Examples of 2-D contour plots of space correlation functions are found in Ukeiley et al. [23]. To measure the space–time distribution of the correlation functions, Bridges and Wernet [24] used two coupled PIV systems (dual PIV) to control the time delay between two velocity snapshots. This was used to measure the space–time correlations of the axial and radial components of velocity in the shear layer of subsonic jets. Thanks to recent breakthroughs, a PIV acquisition at tens of kHz is now possible, though still restricted to small acquisition windows, which is very promising for the measurement of space–time quantities, for example, the time-resolved PIV measurements made by Wernet [25]. Other techniques have also been developed, for instance, the combined use of LDA and PIV by Chatellier and Fitzpatrick [26] and the use of quantitative optical deflectometry by Doty and McLaughlin [27] and Petitjean et al. [28].

However, in spite of the increase in the amount of correlation data in jets, a fine description of the correlation scales is still needed to draw robust conclusions over a wide range of flow conditions. In the most recent studies, the evolution of the correlation scales in the shear layer is usually expressed as a function of the axial distance x_1 . Owing to the earliest studies of Davies et al. [18] and Dimotakis and Brown [20], these results depend on the expansion rate of the shear layer specific to these experiments. The use of these databases as input in acoustic models, for instance, is then limited to the range in which the extrapolation of the measurements is valid, which is not straightforward to predict a priori. Furthermore, to the authors' knowledge, the characterization of the correlations of velocity on the jet axis, especially just downstream of the potential core, is still incomplete.

The aim of the present work is to provide measurements of the space–correlation scales in subsonic isotherm round jets for the axial and radial velocity components, $L_{ii}^{(j)}$, T_{ii} , and T_{cii} . Turbulence is assumed to be stationary in space, and the present results are reported with an appropriate scaling. The ratios between the space and time scales are also analyzed in light of the values expected for homogeneous and isotropic turbulence [15,16]. In the present work, a dual PIV technique is used to explore in detail the shear layer and the jet axis at two Mach numbers, $M = 0.6$ and 0.9 . The jet facility and the instrumentation are described in Sec. II. Section III is devoted to the one-point statistics of turbulence. PIV data are compared with the LDA and pitot tube data for validation. The correlation length scales are provided in Sec. IV and the correlation time scales in Sec. V.

II. Experimental Setup

A. Facility

The experiments were performed in a facility of the Ecole Centrale de Lyon (ECL) designed for acoustic testing of transonic single-stream hot jets. This jet facility is composed of a centrifugal compressor (maximal power of 350 kW, mass-flow rate up to $1 \text{ kg} \cdot \text{s}^{-1}$), an air drier system (power of 12 kW), and of a set of controllable electric resistances (power 64 kW, stagnation temperature $< 500 \text{ K}$). A nozzle of conical shape with an inlet diameter of 90 mm, an exit diameter of $D = 38 \text{ mm}$, an inside face angle of 18 deg, and a lip thickness of 2 mm is used. In this installation, Mach numbers up to 1.6 can be investigated and the static temperature can be kept equal to the ambient temperature for $M < 1.1$. The measurement of the near-field and far-field acoustic spectra over the whole Mach number range of $0.6 < M < 1$ are found in Bogy et al. [29].

In the present study, the aerodynamic characterization of the jet alone is concerned. Two Mach numbers are prescribed, $M = 0.6$ and 0.9 , corresponding to an exit velocity of $U_j = 202$ and $303 \text{ m} \cdot \text{s}^{-1}$, respectively. The temperature is controlled to get isothermal conditions. At the nozzle exit, the Mach number and the static temperature are, respectively, kept with less than 3% variation and 2°C according to the ambient temperature throughout the experiments.

For the use of PIV, the jet is seeded with droplets of olive oil. Eight injectors are located in the settling portion of the jet facility, at 3 m upstream of the nozzle exit and spread out regularly over the circumference of the round tunnel. The injection of the olive-oil spray is made through flush-mounted annular slots to reduce flow distortion. The olive-oil droplets are produced by a homemade generator. The droplet size has been estimated by particle dynamics analysis (PDA) in nearly standard thermodynamic conditions and in the absence of flow and has been found to be less than $1 \mu\text{m}$. To measure the velocity of the ambient flow entrained and mixed in the jet core, the experimentation room is seeded with mineral oil droplets produced by a commercial smoke generator. A similar PIV seeding for jet flows was used by Samimy et al. [30], for instance.

B. Instrumentation

The dual PIV system consists of two coupled conventional PIV systems, as shown in Fig. 1. Each system is composed of a pulsed double-cavity Nd:Yag laser (NewWave Solo PIV III laser or Quantel Brilliant laser, wavelength of 532 nm, energy of 50 mJ/pulse, pulse length of 5 ns, and operating frequency of 4 Hz) and a double-frame charge-coupled device (CCD) camera (PCO SensiCam, 12 bits,

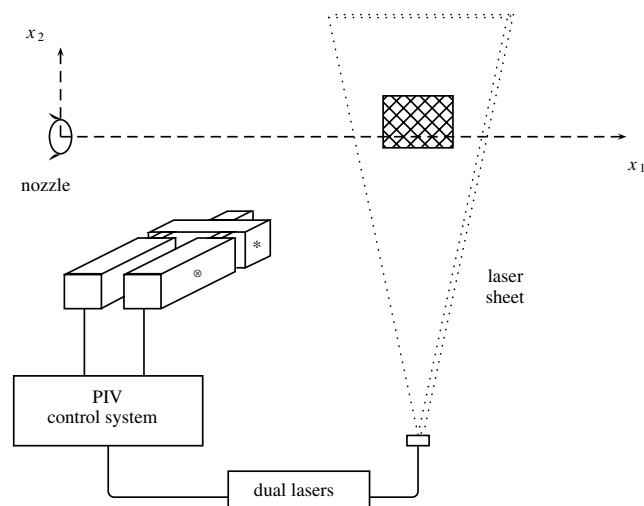


Fig. 1 Sketch of the dual PIV system in the jet facility at the ECL (*: beam splitter and optical shutter, ⊗: two CCD cameras, crosshatch region: recorded view).

1280×1024 pixels). The laser beams are combined by a homemade optical system and then refracted by a cylindrical lens to form a light sheet (2 mm of thickness) propagating across the jet axis. The two cameras are mounted side by side and can be traversed in the axial direction over more than $15D$. A passive beam splitter allows the visualization of the same region of the jet with the two cameras. With a working distance of nearly 600 mm between light sheets and cameras, and using objectives with a focal length of 60 mm, a field of view of $2.2D \times 1.8D$ is obtained. The calibration is performed before operating the jet by recording with both cameras the image of the same calibration plate. Because of the long exposure time of the second frame of CCD cameras (120 ms), a fast optical shutter is used with the first camera. Owing to the small closure delay of the shutter, the firing of both cavities of the second laser is triggered when the shutter is closed, and the second frame of the first camera is not contaminated by spurious diffused light during operation of the second PIV system. With this device, the time lag τ has been lowered to $20 \mu\text{s}$.

The synchronization of the two PIV systems is carried out by a commercial PIV software (DaVis v7.1 from LaVision). The basic acquisition cycle breaks down as follows. Two conventional single PIV acquisitions are operated successively at a time interval of τ . This time lag τ is controlled by the software and has been varied from $20 \mu\text{s}$ (minimal polarization time of the shutter) to $250 \mu\text{s}$ at $M = 0.9$ and $330 \mu\text{s}$ at $M = 0.6$. To obtain $\tau = 0$, the data from one single PIV system are used. The time interval between the two images required for each of the two conventional single PIV acquisitions is $2.5 \mu\text{s}$ for $M = 0.6$ and $1.6 \mu\text{s}$ for $M = 0.9$. After postprocessing, two instantaneous velocity fields time lagged of τ are then obtained. This acquisition cycle is repeated at a frequency of 4 Hz to obtain 2000 velocity field pairs.

The postprocessing of the velocity maps is operated by the PIV software after the acquisition is completed. A multipass algorithm is used, with three steps from the initial window size of 128×128 pixels to the final size of 32×32 pixels ($0.052D \times 0.052D$). Owing to a 50% overlapping of the interrogation windows, around 38 velocity vectors are measured over a distance of $1D$.

III. Single Point Measurements

The validation of the PIV acquisition has been checked with a comparison to the pitot tube and LDA measurements performed in identical flow conditions.

First, the mean axial velocity is analyzed. Radial profiles across the shear layer and longitudinal profiles along the jet axis are given in Fig. 2. The agreement between the different techniques is quite satisfying. Furthermore, the data collapse well with the classical hyperbolic tangent profile in the shear layer:

$$\frac{U_1}{U_a} = 0.5 \left(1 - \tanh \left[\frac{D}{8\delta_\theta} \left(\frac{2x_2}{D} - \frac{D}{2x_2} \right) \right] \right) \quad (4)$$

and with the curve given by the expression

$$\frac{U_1}{U_j} = \frac{1}{(x_1 - L_c)/D + b} \quad (5)$$

far enough downstream on the jet axis. The length of the potential core L_c is $6.5D$ for $M = 0.6$ and $7D$ for $M = 0.9$ in the present measurements. The two constants a and b have been adjusted by a least-mean-square approximation, and the following values $a \approx 0.11$ and $b \approx 0.95$ are found for both Mach numbers.

For the discussion addressed herein, the distribution of the momentum thickness δ_θ is plotted in Fig. 3. For both Mach numbers, δ_θ varies linearly and faster at $M = 0.6$

$$\delta_\theta = 0.0289x_1 + 0.3460 \cdot 10^{-3} \text{ (m)}$$

than at $M = 0.9$

$$\delta_\theta = 0.0265x_1 + 0.1140 \cdot 10^{-3} \text{ (m)}$$

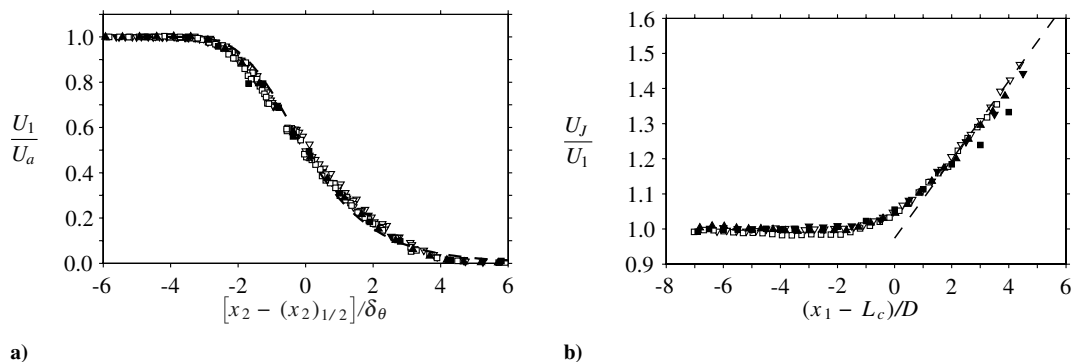


Fig. 2 Axial mean velocity U_1 : a) radial profiles in the shear layer, from $x_1 = D$ to $x_1 = 6D$ every $\Delta x_1 = D/2$; and b) axial profiles on the jet axis. PIV (∇ , \square), LDA (\blacktriangledown \blacksquare), and pitot tube data (\blacktriangle) are superimposed for comparison. The triangle symbols (∇ \blacktriangledown) refer to the $M = 0.6$ jet and the squares (\square , \blacksquare) refer to the $M = 0.9$ jet. The hyperbolic tangent velocity profile (Eq. (4) with $\delta_\theta/D = 0.1$) and the velocity decay law on the jet axis (Eq. (5) with $a = 0.11$ and $b = 0.95$) are also plotted (---) in parts a and b, respectively.

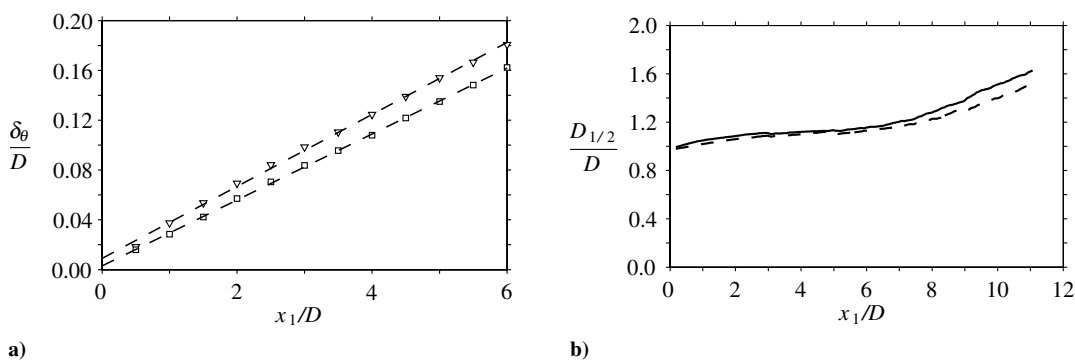


Fig. 3 Distribution of the momentum thickness δ_θ and of the half-velocity diameter $D_{1/2}$: a) $M = 0.6$ (∇) and 0.9 (\square), and b) (—) $M = 0.6$ and (---) 0.9 .

as expected. The distribution of the half-velocity diameter $D_{1/2}$ is also presented in Fig. 3. At the nozzle exit, $D_{1/2}$ coincides with D , and it reaches a constant value slightly higher than D farther downstream over the potential domain $x_1 < L_c$. Downstream of the potential domain, $D_{1/2}$ increases due to the breakdown of the jet.

Second, the fluctuating velocity PIV data are commented upon. In Fig. 4, the radial profiles of the fluctuation of the axial and radial velocities across the shear layer are compared with the LDV measurements. The agreement between the data obtained by the two techniques is satisfying. The maximal rms velocity normalized by U_j is approximately 16% for the axial component and 11% for the radial one.

Fluctuating velocity components on the jet axis are shown in Fig. 5. The agreement between the PIV and LDV is pretty good, with the exception of the axial fluctuating velocity at $M = 0.6$ downstream of the potential core, $x_1 \geq L_c$. In this case, the LDV measurements are questioned owing to the surprising low level of

turbulence obtained compared with the $M = 0.9$ jet. The PIV results, conversely, are comparable for the two Mach numbers. The maximum is reached between 2.5 and $3.5D$ downstream of L_c , with roughly 14.5% and 10.5% for the axial and radial velocity components, respectively.

IV. Space Scales

The space correlation functions $R_{ii}(\mathbf{x}, \boldsymbol{\xi}, \tau = 0)$ have been estimated for a multitude of reference points \mathbf{x} over the first 11 diameters from the nozzle exit, in the shear-layer center ($x_2 = 0.5D$), and along the jet axis ($x_2 = 0$) downstream of the potential core. From this data set, the integral length scales $L_{ii}^{(j)}(\mathbf{x})$ have been calculated. Note that all the integral scales are determined by integration to the first zero crossing instead of the theoretical full integration as explicitly defined in the nomenclature. These results are presented in the following two subsections.

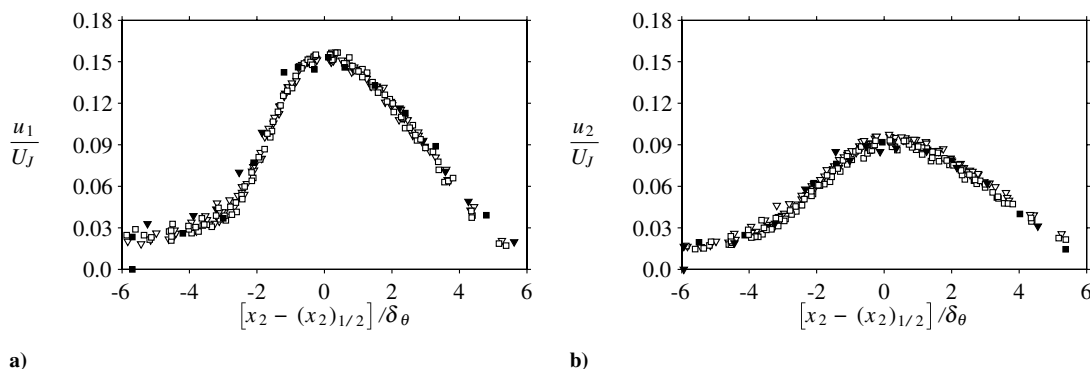


Fig. 4 Radial profiles from $x_1 = 2D$ to $x_1 = 5D$ every $\Delta x_1 = D/2$: a) fluctuating longitudinal velocity, and b) radial velocity. The legend is the same as in Fig. 2.

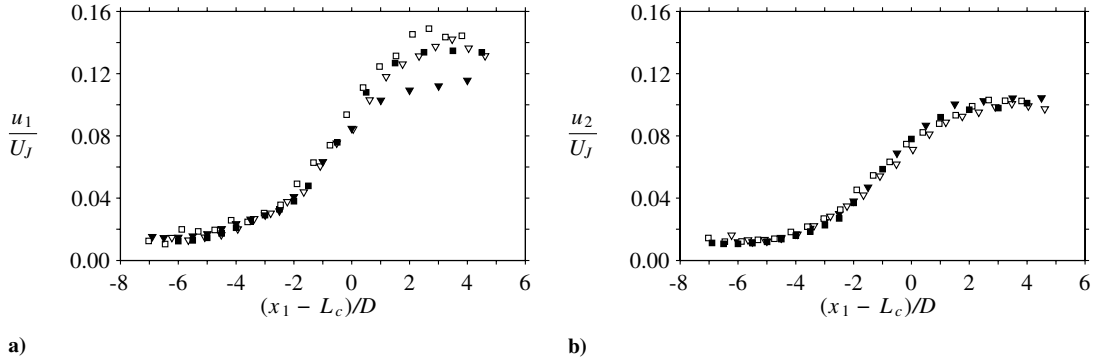


Fig. 5 Axial profiles: a) of the longitudinal velocity, and b) radial velocities. The legend is the same as in Fig. 2.

A. Shear Layer

As an illustration, the space correlation functions R_{11} and R_{22} obtained in the shear layer are shown in Fig. 6. This figure illustrates the quality of the PIV acquisition and the statistical convergence of the data. The complex pattern of the correlation functions R_{11} and R_{22} is also noticeable. The contour plots of R_{11} present two directions along which the low-level and positive values of correlation are stretched and compressed.

These principal directions are distinct from the axial and radial directions and delimit four quadrants of negative correlation levels, $R_{11} < 0$. The principal direction represented by the dashed line in the figure is approximately $\theta = 18$ deg from the axial direction. This angle θ is roughly similar all over the shear layer at the two Mach numbers. Other correlation patterns are available in Fleury [31]. Such an inclination of the isocontours of R_{11} was also highlighted in circular pipe flows by Sabot and Comte-Bellot [32], for instance, and is attributed to the turbulence anisotropy induced by the mean shear flow.

For R_{22} , the isocontours of positive values stretch out only in the radial direction, and two areas of negative correlation level are observed upstream and downstream of the reference point, rather than on the high-speed side of the shear layer. Further downstream, for $x_1 > 2D$, the contour plots of R_{11} and R_{22} stretch around the reference point \mathbf{x} but the pattern is nearly the same.

To illustrate the calculation of the length scales $L_{ii}^{(1)}$, the axial distribution of the correlation functions R_{ii} at $x_1 = 2D$, where $i = 1$ or 2, is plotted in Fig. 7. The integration of R_{ii} is made by a classical trapezoidal method from the experimental data alone, that is, without any extrapolation, and over the domain of positive R_{ii} values around the origin $\xi_1 = 0$. If R_{ii} vanishes outside of the measurement domain, the location of the first zero crossing $\xi_{0i}^{-(1)}$ or $\xi_{0i}^{+(1)}$ is extrapolated linearly from the values in the neighborhood of the window boundary. A similar data analysis is carried out for the radial length scales $L_{ii}^{(2)}$.

The evolution of the correlation length scales $L_{ii}^{(j)}$ in the shear layer is shown in Fig. 8. Several results found in the literature are also superimposed for comparison. A rather poor agreement with the

pioneering results of Laurence [33] and Davies et al. [18] is noticeable for $L_{11}^{(1)}$, whereas a satisfying agreement is found with the data of Liepmann and Laufer [34] concerning $L_{11}^{(2)}$. The more recent data of Lau [21], Jordan and Gervais [35], and Kerhervé et al. [22] collapse better, with the notable exception of the scales $L_{22}^{(j)}$ based on the radial velocity.

The inspection of these results shows the linear evolution of the length scales $L_{ii}^{(j)}$ according to the position along the shear layer. This suggests a linear relation between $L_{ii}^{(j)}$ and the local momentum thickness of the shear layer δ_θ , as supported by the results displayed in Fig. 9. Far enough downstream, remarkable relations are indeed obtained:

$$L_{11}^{(1)} \approx 2\delta_\theta, \quad L_{11}^{(2)} \approx \delta_\theta, \quad \text{and} \quad L_{22}^{(1)} \approx \delta_\theta \quad (6)$$

Such a simple relation cannot be provided for $L_{22}^{(2)}$. Note that Eq. (3), which is derived from Davies’s measurements, is in agreement with the present results.

The self-similarity of the correlation functions in the shear layer is analyzed in light of these results in Fig. 10. The two Mach numbers and two positions of the reference point x_1 are considered. Using the

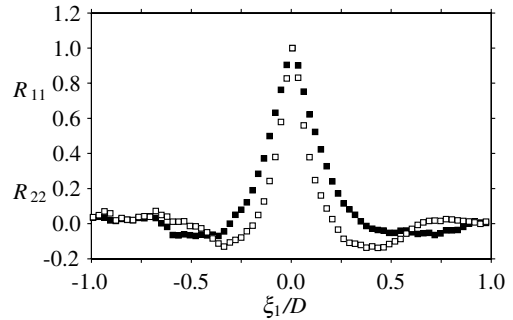


Fig. 7 Axial distribution ($\xi_2 = 0$) of the space correlation functions R_{11} (■) and R_{22} (□) in the shear layer at $(x_1, x_2) = (2D, 0.5D)$ for $M = 0.9$.

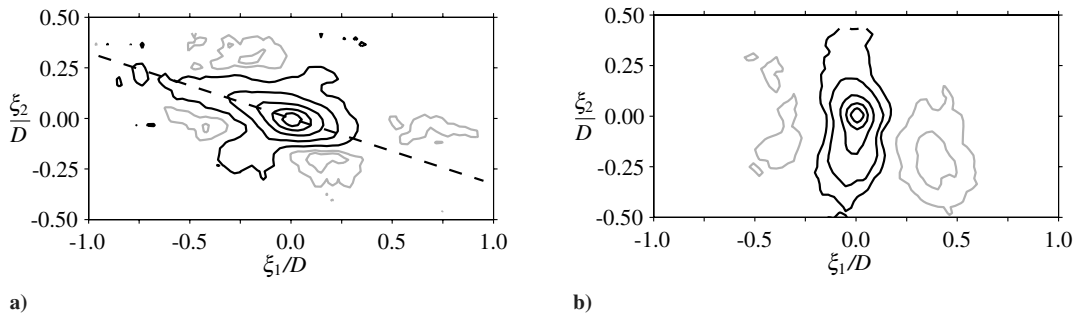


Fig. 6 Isocontours of the space correlation functions in the shear layer, at $(x_1, x_2) = (2D, 0.5D)$ for $M = 0.9$: a) $R_{11}(x, \xi, \tau = 0)$, and b) $R_{22}(x, \xi, \tau = 0)$. The R_{11} -correlation levels are 0.8, 0.6, 0.4, 0.2, and 0.05 in black and -0.05 and -0.1 in gray. The R_{22} -correlation levels are 0.8, 0.6, 0.4, 0.2, and 0.1 in black and -0.1 and -0.2 in gray.

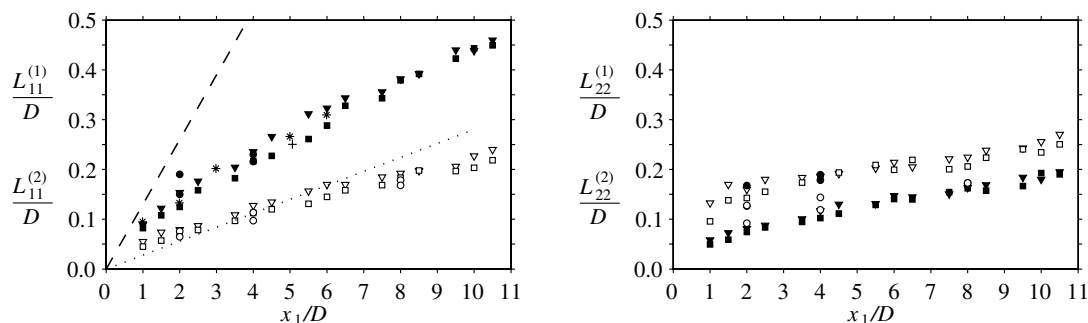


Fig. 8 Correlation length scales in the shear-layer center ($x_2 = 0.5D$) for $M = 0.6$ (∇ , \blacktriangledown) and 0.9 (\square , \blacksquare). The following measurements are also superimposed: (...) Laurence [33] and Davies et al. [18] ($L_{11}^{(1)} = 0.13x_1$); (—) Liepmann and Laufer [34] ($L_{11}^{(2)} = 0.028x_1$); (+) Jordan and Gervais [35] ($M = 0.75$); (\circ , \bullet) Lau [21] ($M = 0.5$ and 0.9); (*) Kerhervé [22] (perfectly expanded jet at $M = 1.2$). The black symbols stand for the axial direction, $L_{ii}^{(1)}$ and the open ones for the radial direction, $L_{ii}^{(2)}$.

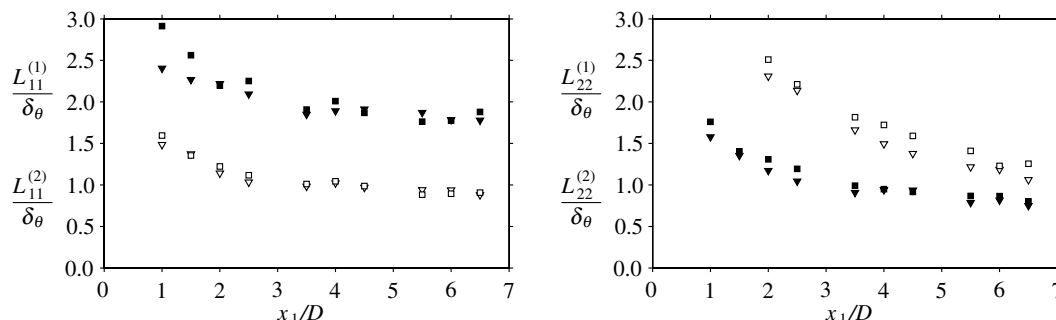


Fig. 9 Ratio between the correlation length scales in the shear layer and the local momentum thickness δ_θ for $M = 0.6$ and 0.9 . The legend is the same as in Fig. 8.

reduced variables ξ_1/D and ξ_2/D , the R_{11} plots do not collapse. Conversely, with the reference length δ_θ , a quasi self-similarity of the R_{11} function is obtained. The R_{22} function is also plotted in Fig. 10, and the conclusions are the same in the axial direction: R_{22} is self-similar according to the reduced variable ξ_1/δ_θ . The distribution of R_{22} in the radial direction, however, is more subtle. In the low-speed side of the shear layer for $\xi_2 \geq 0$ the appropriate reduced variable is ξ_2/δ_θ , but in the high-speed side for $\xi_2 < \delta_\theta$ the appropriate reference length is rather the diameter D . This explains why the length scale $L_{22}^{(2)}$ is neither well scaled by D nor by δ_θ alone.

For isotropic turbulence, specific relations between the length scales are expected (see Batchelor [15] and Townsend [16]):

$$L_{11}^{(1)}/L_{22}^{(2)} = 1 \quad \text{and} \quad L_{11}^{(2)}/L_{22}^{(1)} = 1 \quad (7)$$

$$L_{11}^{(1)}/L_{11}^{(2)} = 2 \quad \text{and} \quad L_{22}^{(2)}/L_{22}^{(1)} = 2 \quad (8)$$

These isotropic ratios are tested in Fig. 11. The relations (7) and (8), which do not involve the length scale $L_{22}^{(2)}$, are roughly well satisfied, in spite of the anisotropy of the turbulence in the shear layer. As $L_{22}^{(2)}$ is involved, the isotropic ratios cannot be constant as $L_{22}^{(2)}$ does not scale according to δ_θ , conversely to the other correlation scales. Surprisingly, the ratios $L_{11}^{(1)}/L_{22}^{(2)}$ and $L_{22}^{(2)}/L_{22}^{(1)}$ do not strongly deviate from the values expected in isotropic turbulence.

B. Jet Axis

An example of the space correlation functions R_{11} and R_{22} obtained on the jet axis is shown in Fig. 12. The isocontours of R_{11} and R_{22} are aligned along orthogonal directions, in the axial direction for R_{11} and in the radial direction for R_{22} . Negative correlation regions are also noticed on the two sides of the stretching directions, that is, in the $\xi_2 > 0$ and $\xi_2 < 0$ regions for R_{11} and in the $\xi_1 < 0$ and $\xi_1 > 0$ regions for R_{22} . This type of correlation pattern has been observed all over the jet axis, far enough downstream of the potential

core. At the end of the potential core, $x_1 = L_c$, the regions of negative correlation levels of R_{11} are turned by 90 deg with regard to the present illustration and are thus on the $\xi_1 < 0$ and $\xi_1 > 0$ sides (see Fleury [31]).

The integral length scales associated with R_{11} and R_{22} have been calculated as earlier in Sec. IV.A. The results are plotted in Fig. 13. They are presented in terms of the jet diameter D and the half-velocity diameter $D_{1/2}$. As $D_{1/2}$ is used to normalize the length scales $L_{11}^{(j)}$ associated with the axial fluctuating velocity, a roughly constant value is reached downstream of the potential core, the same for the two Mach numbers:

$$L_{11}^{(1)} \approx 0.25D_{1/2} \quad \text{and} \quad L_{11}^{(2)} \approx 0.11D_{1/2} \quad (9)$$

For the length scales $L_{22}^{(j)}$ associated with the radial velocity, the results are too scattered to draw unambiguous conclusions. Owing to the data on $L_{22}^{(2)}$, it seems, however, that D should be the appropriate reference length, with

$$L_{22}^{(1)} \approx 0.17D \quad (10)$$

far enough downstream.

The self-similarity of the correlation functions on the jet axis is analyzed in Fig. 14. The plots of the correlation function R_{11} obtained at $x_1 = 7.5D$ and $10.5D$ for the two Mach numbers do collapse when $D_{1/2}$ is used as the reference length. This is in agreement with the scaling of $L_{11}^{(j)}$ according to $D_{1/2}$. Unfortunately, a close insight into the distribution of the correlation function R_{22} does not provide a reliable indication as to the most appropriate reduced variable to use, ξ_i/D or $\xi_i/D_{1/2}$. The two locations of the reference point, $x_1 = 7.5D$ and $10.5D$, are too close to conclude and further measurements are needed.

The isotropic ratios of the integral length scales are investigated in Fig. 15. Although the isotropic ratios are not constant, they do not indicate a strong anisotropy of the integral length scales. Far enough

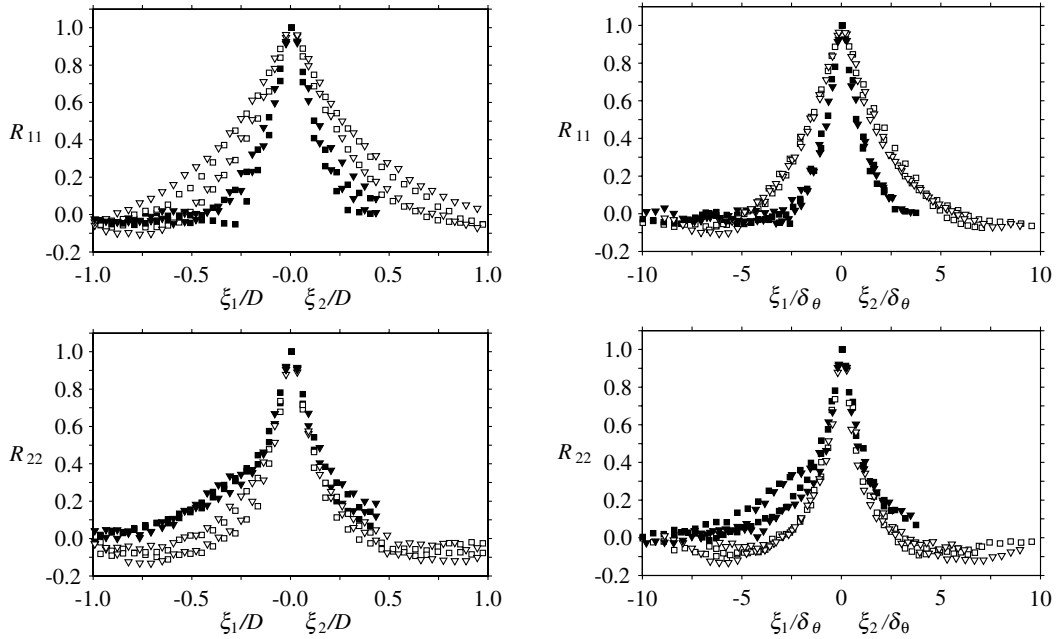


Fig. 10 Self-similarity of the space correlation functions in the center of the shear layer ($x_2 = 0.5D$), in the longitudinal direction ξ_1 (open symbols) and in the radial direction ξ_2 (black symbols). The two Mach numbers and two positions of the reference point, $x_1 = 4D$ and $x_1 = 6D$, are considered. The legend is the same as in Fig. 8.

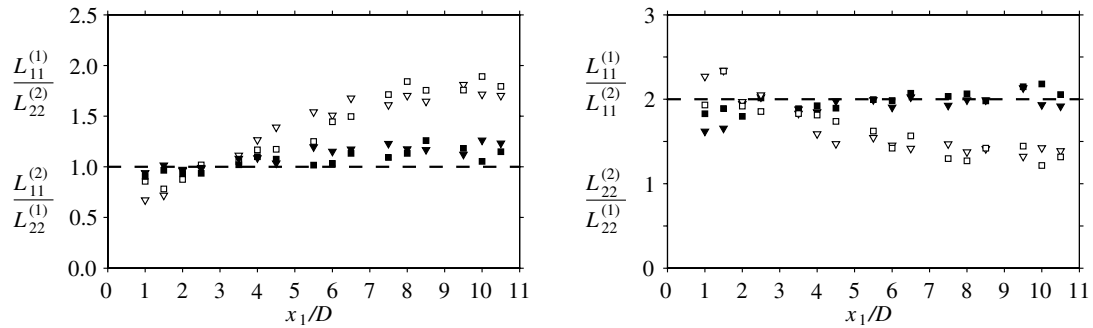


Fig. 11 Isotropic ratios between the correlation length scales in the shear layer for $M = 0.6$ (∇ , \blacktriangledown) and 0.9 (\square , \blacksquare). On the left-hand side, the black symbols stand for $L_{11}^{(2)}/L_{22}^{(1)}$ and the open symbols for $L_{11}^{(1)}/L_{22}^{(2)}$. On the right-hand side, the black symbols stand for $L_{11}^{(1)}/L_{11}^{(2)}$ and the open symbols for $L_{22}^{(2)}/L_{22}^{(1)}$.

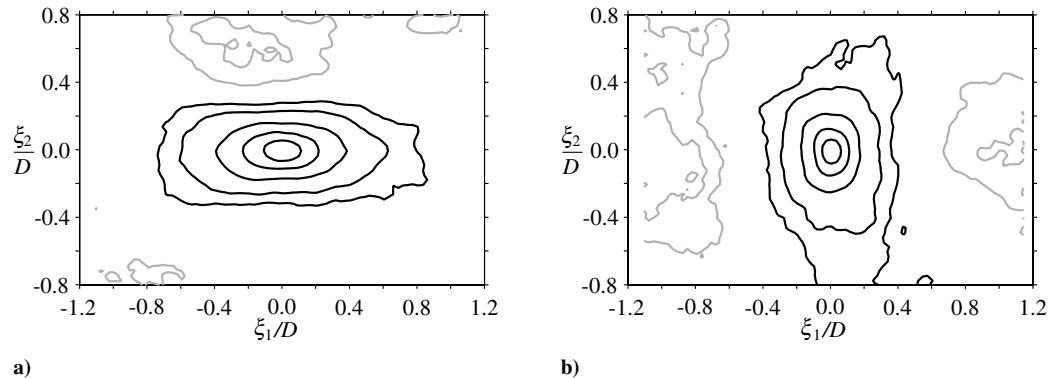


Fig. 12 Isocontour of the space correlation functions on the jet axis ($x_2 = 0$) at $x_1 = 10D$ and $M = 0.9$: a) $R_{11}(x, \xi, \tau = 0)$, and b) $R_{22}(x, \xi, \tau = 0)$. The correlation levels are 0.8, 0.6, 0.4, 0.2, and 0.1 in black and -0.05 and -0.1 in gray.

downstream, the following relations are obtained:

$$L_{11}^{(1)}/L_{22}^{(2)} = 0.9 \quad \text{and} \quad L_{11}^{(2)}/L_{22}^{(1)} = 1.5 \quad (11)$$

$$L_{11}^{(1)}/L_{11}^{(2)} = 2.4 \quad \text{and} \quad L_{22}^{(2)}/L_{22}^{(1)} = 1.5 \quad (12)$$

V. Time Scales

Because of the large amount of data required for the analysis of time correlation functions, the space-time measurements are only reported for three regions in the shear layer, around $x_1 = 4.5D$, $6.5D$, and $10.5D$, respectively.

As an illustration, the contour plots of R_{11} and R_{22} in the shear layer at $x_1 = 6.5D$ and for the jet at Mach number $M = 0.9$ are

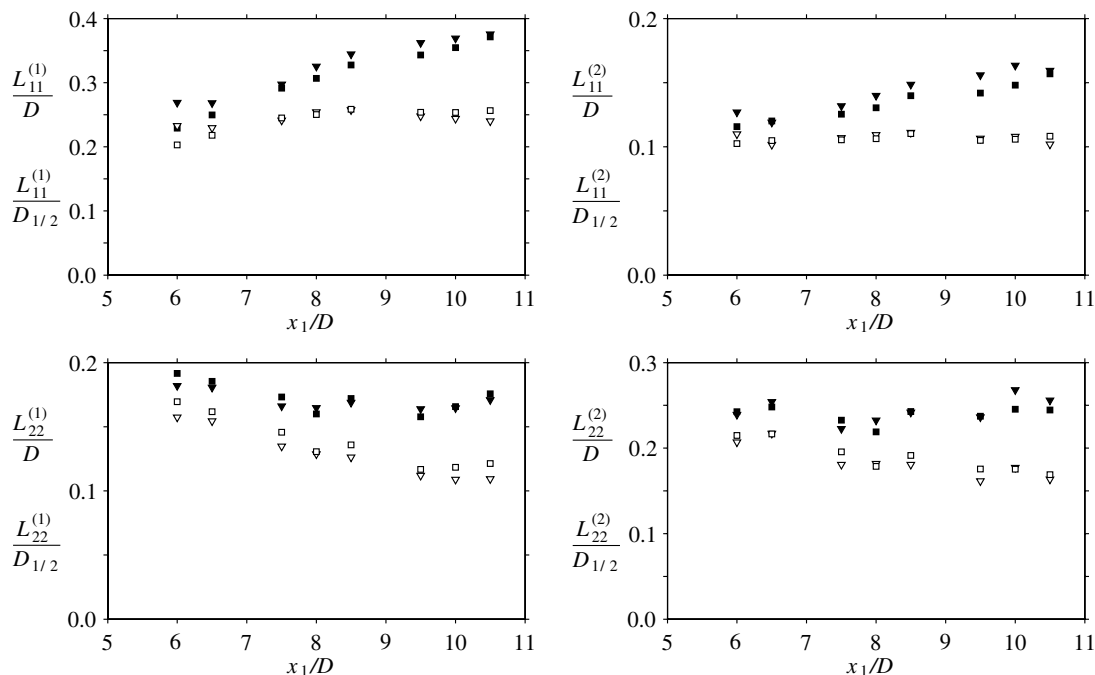


Fig. 13 Correlation length scales on the jet axis ($x_2 = 0$) $M = 0.6$ ($\nabla, \blacktriangledown$) and 0.9 (\square, \blacksquare). The black symbols stand for the normalization of integral length scales by D and the open ones for the normalization by $D_{1/2}$.

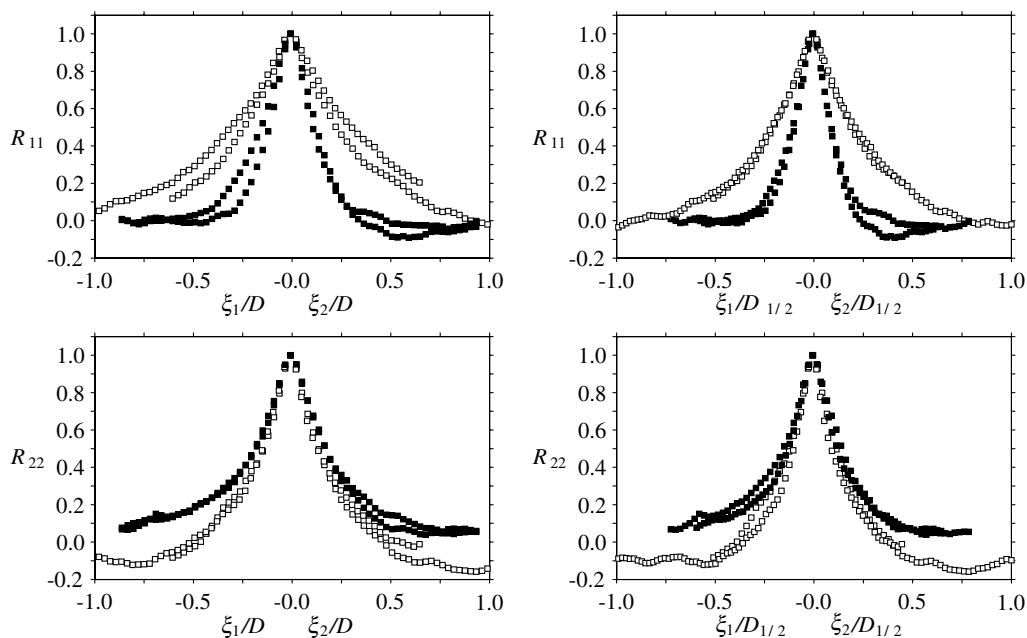


Fig. 14 Similarity of the space correlation functions on the jet axis ($x_2 = 0$) in the longitudinal direction ξ_1 (open symbols) and in the radial direction ξ_2 (black symbols). Two positions are considered for the reference point, $x_1 = 7.5D$ and $10.5D$ ($M = 0.9$).

displayed in Fig. 16 for different time lags τ . The convection and the attenuation of the correlation patterns are clearly visible. Furthermore, the inclination angle θ of the R_{11} correlation pattern does not vary with τ .

For the same reference point and condition, namely, $(x_1, x_2) = (6.5D, 0.5D)$ and $M = 0.9$, the location of the maximum correlation ξ_c has been followed with respect to the time lag τ . Both R_{11} and R_{22} have been considered. This separation vector ξ_c is taken along the axial direction, and ξ_{c1} is provided in Fig. 17. As expected, the location of the maximum correlation ξ_{c1} is identical for R_{11} and R_{22} and moves linearly according to τ . From this curve, a convection velocity $U_c = \xi_{c1}/\tau$ of the correlation pattern can be deduced. The result is provided in Table 1 for the different reference points and for the two Mach numbers. In all the cases, a convection velocity

between 0.6 and $0.7U_a(x_1)$ is obtained, as is classically found in axisymmetrical shear layers.

Two integral time scales are usually associated with the time attenuation of the correlation functions. The first one, T_{cii} , is the reference time of the correlation function in the convected frame $R_{ii}(\mathbf{x}, \xi = U_c \tau, \tau)$, that is, of the attenuation of the maximum correlation. The second one, T_{ii} , is the characteristic time of the correlation function at the reference point $R_{ii}(\mathbf{x}, \xi = 0, \tau)$. By definition, it follows that $R_{ii}(\mathbf{x}, \xi = U_c \tau, \tau) \geq R_{ii}(\mathbf{x}, \xi = 0, \tau)$, and thus $T_{cii} \geq T_{ii}$. To illustrate the calculation of these time scales, an example of correlation functions $R_{ii}(\mathbf{x}, \xi = 0, \tau)$ and $R_{ii}(\mathbf{x}, \xi = U_c \tau, \tau)$ measured in the shear layer at $(x_1, x_2) = (6.5D, 0.5D)$ and for $M = 0.9$ is reported in Fig. 18. Because no data are available for time delays larger than $300 \mu s$ corresponding roughly to a

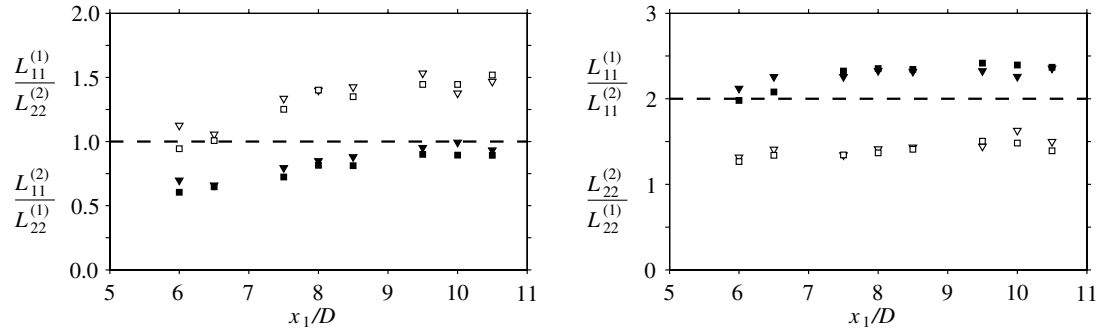


Fig. 15 Isotropic ratios between the correlation length scales on the jet axis at $M = 0.6$ and 0.9 . The legend is the same as in Fig. 11.

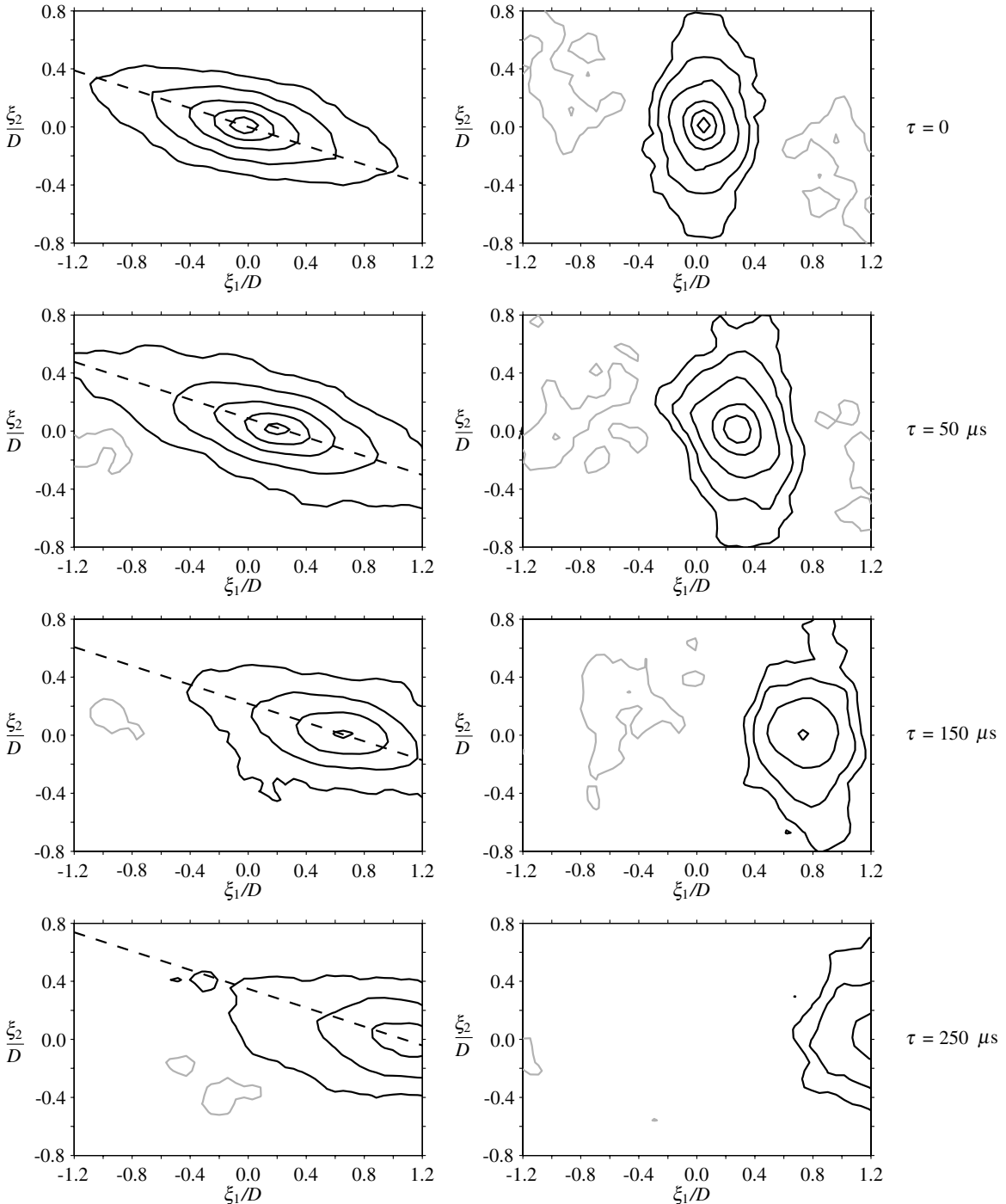


Fig. 16 Space-time correlation functions for $R_{11}(x, \xi, \tau)$ along the left-hand side and $R_{22}(x, \xi, \tau)$ along the right-hand side in the shear-layer center ($x_2 = 0.5D$) at $x_1 = 6.5D$ and $M = 0.9$. The correlation levels are 0.8, 0.6, 0.4, 0.2, and 0.05 in black and -0.05 and -0.1 in gray for R_{11} and 0.8, 0.6, 0.4, 0.2, and 0.1 in black and -0.1 and -0.2 in gray for R_{22} .

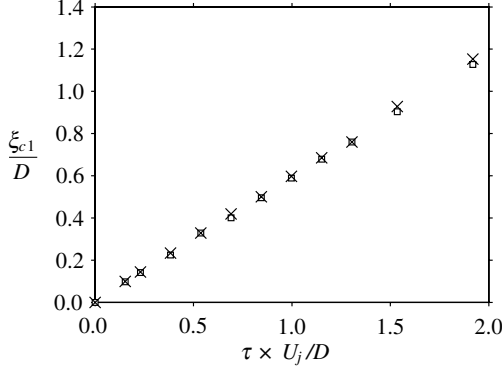


Fig. 17 Separation corresponding to the maximum of R_{11} (\square) and R_{22} (\times) in the convected frame, according to the time delay τ . The reference point (x_1, x_2) is located in the shear-layer center $(6.5D, 0.5D)$, jet at Mach number $M = 0.9$.

nondimensional time $2D/U_j$, the integral time scales T_{cii} are estimated by extrapolation using a classical exponential function:

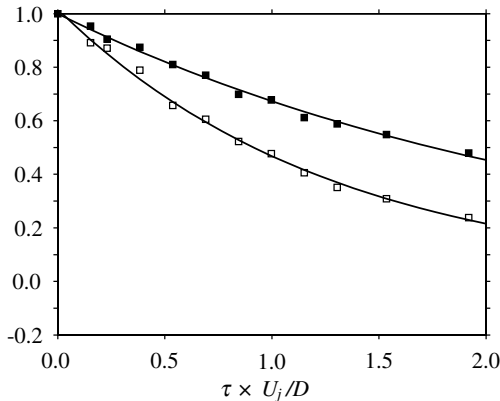
$$R_{ii}(\mathbf{x}, \xi = \mathbf{U}_c \tau, \tau) \approx \exp\left(-\frac{\tau}{T_{cii}}\right) \quad (13)$$

This function is actually a good approximation of the present measurements as also shown in Fig. 18a, and T_{cii} is estimated from the best least-mean-square approximation. The evaluation of the time scale T_{ii} is obtained by the integration of the data over the positive correlation range $R_{ii}(\mathbf{x}, \xi = 0, \tau) > 0$, with possibly linear extrapolation to the first zero crossing, as performed for length scales in the previous section. The results are provided in Table 2. It is found that T_{cii} and T_{ii} are linked to the local reference times Θ_{cii} and Θ_{ii} , respectively, according to the remarkable relations

$$T_{cii} \approx \Theta_{cii} \quad T_{ii} \approx \Theta_{ii} \quad (14)$$

The first relation is in agreement with the dimensional analysis yielding Eq. (3). Such a simple relation between T_{cii} and Θ_{cii} , with a scaling factor close to unity, also fits the results obtained for other flows, such as the inner region of boundary layers and the circular pipe flows (see Kovaszny et al. [36] and Sabot et al. [37], respectively).

From the convection velocity U_c and the correlation time scale in the convected frame T_{cii} , one can define a length $L_{cii} = U_c T_{cii}$. This length scale may be interpreted as the interval over which the fluctuation of velocity u_i remains correlated during the convection of turbulent structures. These data are reported in Table 3. Roughly, L_{c11} is between 1 and 2 diameters from $x_1 = 4.5$ to $10.5D$ in the shear-layer center, and L_{c22} between 0.7 and $1.0D$. Furthermore,



a)

Table 1 Convection velocity U_c in the shear-layer center ($x_2 = 0.5D$)

$M = 0.6$			$M = 0.9$		
x_1	U_c	U_c/U_a	x_1	U_c	U_c/U_a
$4.5D$	—	—	$4.5D$	$175 \text{ m} \cdot \text{s}^{-1}$	0.6
$6.5D$	$110 \text{ m} \cdot \text{s}^{-1}$	0.6	$6.5D$	$170 \text{ m} \cdot \text{s}^{-1}$	0.6
$10.5D$	$97 \text{ m} \cdot \text{s}^{-1}$	0.7	$10.5D$	$152 \text{ m} \cdot \text{s}^{-1}$	0.7

these scales grow in the downstream direction due to the decrease of the shear intensity. Though only fairly constant, the ratio $L_{cii}/L_{ii}^{(1)}$ is between 4 and 5 for $i = 1$ and between 5 and 6 for $i = 2$.

The relationships between the time scales in the fixed frame T_{ii} and the ones in the convected frame T_{cii} are finally investigated in Table 4. Owing to Eq. (14) and the results provided in Sec. III, it is expected that

$$\frac{T_{11}}{T_{c11}} \approx \frac{u_1}{U_1} = \frac{u_1 U_a}{U_a U_1} \approx 0.16 \times 2 = 0.32$$

and

$$\frac{T_{22}}{T_{c22}} \approx \frac{u_2}{U_1} = \frac{u_2 U_a}{U_a U_1} \approx 0.11 \times 2 = 0.22$$

which is in reasonable agreement with the experimental results. Our data are also in fair agreement with the results found in Kerhervé et al. [22] (see their Table 2), $T_{11} \approx T_{c11}/4.7 \approx 0.21T_{c11}$.

Moreover, in the case of isotropic turbulence, Eq. (14) implies the following relationships between the time scales associated with the radial and axial velocity components:

$$\frac{T_{c22}}{T_{c11}} = \frac{u_1 L_{22}^{(1)}}{u_2 L_{11}^{(1)}} = \frac{L_{22}^{(1)}}{L_{11}^{(1)}} = \frac{1}{2} \quad (15)$$

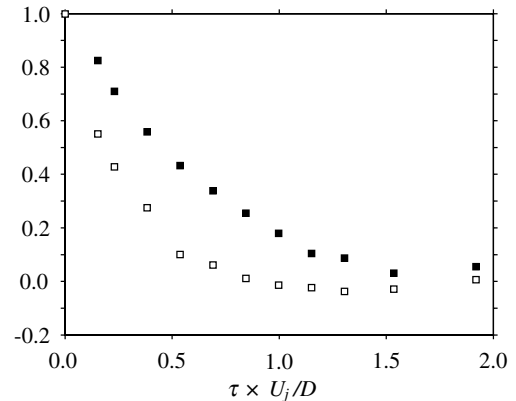
and:

$$\frac{T_{22}}{T_{11}} = \frac{L_{22}^{(1)}}{L_{11}^{(1)}} = \frac{1}{2} \quad (16)$$

The experimental value of these ratios is also provided in Table 4. As noticed, the integral time scales closely satisfy the required relations for isotropy or, at least, do not present a strong anisotropy.

VI. Conclusions

Dual PIV measurements have been carried out in Mach 0.6 and 0.9 isotherm single-stream jets to characterize the space–time correlation scales of the radial and axial velocity components. The shear-layer center and the jet axis have been explored in detail. To provide robust



b)

Fig. 18 Attenuation of the correlation in the shear-layer center ($x_2 = 0.5D$) at $x_1 = 6.5D$ and for $M = 0.9$: a) in the convected frame $R_{ii}(\mathbf{x}, \xi = \mathbf{U}_c \tau, \tau)$, and b) in a fixed frame $R_{ii}(\mathbf{x}, \xi = 0, \tau)$. The black symbols stand for the axial velocity R_{11} , the open ones for the radial velocity R_{22} , and the solid lines for the exponential extrapolation (13).

Table 2 Time scales in the shear layer

	x_1	T_{c11}	T_{c11}/Θ_{c11}	T_{c22}	T_{c22}/Θ_{c22}	T_{11}	T_{11}/Θ_{11}	T_{22}	T_{22}/Θ_{22}
$M = 0.6$	4.5D	—	—	—	—	—	—	—	—
	6.5D	511 μs	1.2	260 μs	0.90	121 μs	1.1	56.0 μs	1.1
	10.5D	712 μs	1.1	396 μs	1.1	172 μs	0.9	80.4 μs	1.1
$M = 0.9$	4.5D	249 μs	1.4	148 μs	1.1	57.0 μs	1.4	28.8	1.4
	6.5D	329 μs	1.3	168 μs	0.99	77.2 μs	1.2	33.6	1.1
	10.5D	451 μs	1.2	235 μs	1.0	117 μs	1.1	51.2	1.1

Table 3 Integral time scales

$M = 0.6$					$M = 0.9$				
x_1	L_{c11}/D	L_{c22}/D	$L_{c11}/L_{11}^{(1)}$	$L_{c22}/L_{22}^{(1)}$	x_1	L_{c11}/D	L_{c22}/D	$L_{c11}/L_{11}^{(1)}$	$L_{c22}/L_{22}^{(1)}$
4.5D	—	—	—	—	4.5D	1.1	0.68	5.0	6.1
6.5D	1.5	0.75	4.3	5.2	6.5D	1.5	0.75	4.5	5.4
10.5D	1.8	1.0	3.9	5.2	10.5D	1.8	0.94	4.0	4.9

Table 4 Ratios between the time scales in the shear layer

$M = 0.6$					$M = 0.9$				
x_1	T_{c22}/T_{c11}	T_{22}/T_{11}	T_{11}/T_{c11}	T_{22}/T_{c22}	x_1	T_{c22}/T_{c11}	T_{22}/T_{11}	T_{11}/T_{c11}	T_{22}/T_{c22}
4.5D	—	—	—	—	4.5D	0.59	0.51	0.23	0.19
6.5D	0.51	0.46	0.24	0.21	6.5D	0.51	0.43	0.23	0.20
10.5D	0.56	0.47	0.24	0.20	10.5D	0.52	0.44	0.26	0.22

results for a large range of flow conditions, the integral scales have been provided as a function of appropriate quantities.

The length scales in the shear layer depend on the local momentum thickness δ_θ according to simple linear relations, except for $L_{22}^{(2)}$, which follows a more subtle evolution. These relations are, however, valid far enough downstream only. On the jet axis, the half-velocity diameter $D_{1/2}$ is the suitable reference length to normalize the integral length scales $L_{11}^{(i)}$. For $L_{22}^{(i)}$, neither D nor $D_{1/2}$ are perfectly suited for the scaling. The self-similarity of the correlation functions in the shear layer and on the jet axis has been obtained by using the reduced variables based on the appropriate reference lengths obtained experimentally. The time scales in the shear layer depend on the reference time defined from the momentum thickness and the mean or rms local velocity regarding the time scale in the fixed frame T_{ii} or the time scale in the convected frame T_{cii} , respectively. Surprisingly, isotropic ratios between these different length or time integral scales have been recovered. The inclination of the correlation pattern R_{11} in the shear layer was also observed. Regarding these results, a possible expression of the correlation R_{11} , which is required in aeroacoustic statistical models for instance, could be written in the following form:

$$R_{11}(\mathbf{x}, \xi, \tau) = f\left(P_\theta \begin{bmatrix} \xi_1/L_{11}^{(1')} \\ \xi_2/L_{11}^{(2')} \end{bmatrix}\right) g\left(\frac{\tau}{T_{11} \text{ or } T_{c11}}\right)$$

where P_θ is the rotation operator by angle $\theta \approx 18$ deg, and $L_{11}^{(i')}$ are the correlation scales in the principal axes of the mean shear flow. The influence of this inclination on the radiated acoustic field through statistical models seems, however, unclear at the present time.

Acknowledgments

The authors gratefully acknowledge J.-M. Perrin, N. Grosjean, P. Souchotte, and P. Roland for their technical assistance and G. Comte-Bellot for her careful rereading and helpful discussions. This work was partially supported by the Centre National d'Etudes Spatiales (CNES).

References

- [1] Proudman, J., "The Generation of Noise by Isotropic Turbulence," *Proceedings of the Royal Society of London, Series A*, Vol. 214, No. 1116, Aug. 1952, pp. 119–132. doi:10.1098/rspa.1952.0154
- [2] Lighthill, M. J., "On Sound Generated Aerodynamically. I. General Theory," *Proceedings of the Physical Society of London, Series A*, Vol. 211, No. 1107, March 1952, pp. 564–587.
- [3] Lighthill, M. J., "On Sound Generated Aerodynamically. II. Turbulence as a Source of Sound," *Proceedings of the Physical Society of London, Series A*, Vol. 222, No. 1148, Feb. 1954, pp. 1–32.
- [4] Ribner, H. S., "Quadrupole Correlations Governing the Pattern of Jet Noise," *Journal of Fluid Mechanics*, Vol. 77, No. 3, 1976, pp. 511–529. doi:10.1017/S0022112076002231
- [5] Béchara, W., Lafon, P., Bailly, C., and Candel, S., "Application of a $k-\epsilon$ Model to the Prediction of Noise for Simple and Coaxial Free Jets," *Journal of the Acoustical Society of America*, Vol. 97, No. 6, 1995, pp. 3518–3531. doi:10.1121/1.412438
- [6] Bailly, C., Lafon, P., and Candel, S., "Subsonic and Supersonic Jet Noise Predictions from Statistical Source Models," *AIAA Journal*, Vol. 35, No. 11, 1997, pp. 1688–1696.
- [7] Khavaran, A., "Role of Anisotropy in Turbulent Mixing Layer," *AIAA Journal*, Vol. 37, No. 7, 1999, pp. 832–841.
- [8] Morris, P. J., and Farassat, F., "Two-Point Cross Correlations of Turbulence and Noise Predictions: Analysis and Simulation," *AIAA Journal*, Vol. 40, No. 4, 2002, pp. 671–680.
- [9] Ribner, H. S., "On Spectra and Directivity of Jet Noise," *Journal of the Acoustical Society of America*, Vol. 35, No. 4, April 1963, pp. 614–616. doi:10.1121/1.1918565
- [10] Goldstein, M. E., and Rosenbaum, B., "Effect of Anisotropic Turbulence on Aerodynamic Noise," *Journal of the Acoustical Society of America*, Vol. 54, No. 3, Sept. 1973, pp. 630–645. doi:10.1121/1.1913643
- [11] Morris, J. P., Boluriaan, S., Lilley, G. M., and Long, L. N., "Two-Point Cross Correlations of Turbulence and Noise Predictions: Analysis and Simulation," AIAA Paper 2002-0071, 2002.
- [12] He, G.-W., Wang, M., and Lele, S., "On the Computation of Space-Time Correlations by Large-Eddy Simulation," *Physics of Fluids*, Vol. 16, No. 11, 2004, pp. 3859–3867. doi:10.1063/1.1779251

- [13] Bailly, C., and Comte-Bellot, G., *Turbulence*, CNRS Editions, Paris, 2003, ISBN 2-271-06008-7.
- [14] Comte-Bellot, G., and Corrsin, S., "The Use of a Contraction to Improve the Isotropy of Grid-Generated Turbulence," *Journal of Fluid Mechanics*, Vol. 25, No. 4, 1966, pp. 657–682. doi:10.1017/S0022112066000338
- [15] Batchelor, G. K., *The Theory of Homogeneous Turbulence*, Cambridge Univ. Press, Cambridge, England, U.K., 1953.
- [16] Townsend, A. A., "The Measurement of Double and Triple Correlation Derivatives in Isotropic Turbulence," *Proceedings of the Cambridge Philosophical Society (Mathematical and Physical Sciences)*, Vol. 43, No. 2, 1947, p. 560.
- [17] Comte-Bellot, G., and Corrsin, S., "Simple Eulerian Time Correlation of Full- and Narrow-Band Velocity Signals in Grid-Generated, 'Isotropic' Turbulence," *Journal of Fluid Mechanics*, Vol. 48, No. 2, 1971, pp. 273–337. doi:10.1017/S0022112071001599
- [18] Davies, P. O. A. L., Fisher, M. J., and Barratt, M. J., "The Characteristics of the Turbulence in the Mixing Region of a Round Jet," *Journal of Fluid Mechanics*, Vol. 15, 1963, pp. 337–367. doi:10.1017/S0022112063000306
- [19] Lau, J. C., Morris, P. J., and Fisher, M. J., "Measurements in Subsonic and Supersonic Free Jets Using Laser Velocimeter," *Journal of Fluid Mechanics*, Vol. 93, No. 1, 1979, pp. 1–27. doi:10.1017/S0022112079001750
- [20] Dimotakis, P. E., and Brown, G. L., "The Mixing Layer at High Reynolds Number: Large-Structure Dynamics and Entrainment," *Journal of Fluid Mechanics*, Vol. 78, No. 3, 1976, pp. 535–560. doi:10.1017/S0022112076002590
- [21] Lau, J. C., "Laser Velocimeter Correlation Measurements in Subsonic and Supersonic Jets," *Journal of Sound and Vibration*, Vol. 70, No. 1, 1980, pp. 85–101. doi:10.1016/0022-460X(80)90556-8
- [22] Kerhervé, F., Jordan, P., Gervais, Y., Valière, J.-C., and Braud, P., "Two-Point Laser Doppler Velocimetry Measurements in a Mach 1.2 Cold Supersonic Jet for Statistical Aeroacoustic Source Model," *Experiments in Fluids*, Vol. 37, No. 3, Sept. 2004, pp. 419–437. doi:10.1007/s00348-004-0815-1
- [23] Ukeiley, L., Tinney, C. E., Mann, R., and Glauser, M., "Spatial Correlations in a Transonic Jet," *AIAA Journal*, Vol. 45, No. 6, 2007, pp. 1357–1369. doi:10.2514/1.26071
- [24] Bridges, J., and Wernet, M. P., "Measurements of the Aeroacoustic Sound Source in Hot Jets," AIAA Paper 2003-3130, May 2003.
- [25] Wernet, M. P., "Temporally Resolved PIV for Space-Time Correlations in Both Cold and Hot Jet Flows," *Measurement Science and Technology*, Vol. 18, No. 5, May 2007, pp. 1387–1403. doi:10.1088/0957-0233/18/5/027
- [26] Chatellier, L., and Fitzpatrick, J., "Spatio-Temporal Correlation Analysis of Turbulent Flows Using Global and Single-Point Measurements," *Experiments in Fluids*, Vol. 38, No. 5, May 2005, pp. 563–575. doi:10.1007/s00348-004-0910-3
- [27] Doty, M. J., and McLaughlin, D. K., "Space-Time Correlation Measurements of High-Speed Axisymmetric Jets Using Optical Deflectometry," *Experiments in Fluids*, Vol. 38, No. 4, 2005, pp. 415–425. doi:10.1007/s00348-004-0920-1
- [28] Petitjean, B. P., Viswanathan, K., McLaughlin, D. K., and Morris, P. J., "Space-Time Correlation Measurements in Subsonic and Supersonic Jets Using Deflectometry," AIAA Paper 2007-36132007.
- [29] Bogey, C., Barré, S., Fleury, V., Bailly, C., and Juvé, D., "Experimental Study of the Spectral Properties of Near-Field and Far-Field Jet Noise," *International Journal of Aeroacoustics*, Vol. 6, No. 2, April 2007, pp. 73–92. doi:10.1260/147547207781041868
- [30] Samimy, M., Kim, J.-H., Kastner, J., Adamovich, I., and Utkin, Y., "Active Control of High-Speed and High-Reynolds-Number Jets Using Plasma Actuators," *Journal of Fluid Mechanics*, Vol. 578, May 2007, pp. 305–330. doi:10.1017/S0022112007004867
- [31] Fleury, V., *Superdirectivité, Bruit d'Appariement et Autres Contributions au Bruit de Jet Subsonique*, Ph.D. Thesis, Ecole Centrale de Lyon, Ecully, France, 2006.
- [32] Sabot, J., and Comte-Bellot, G., "Courbes d'Iso-Corrélations Spatiales et d'Iso-Corrélations Temporelles Relatives aux Fluctuations Longitudinales de Vitesse en Conduite Lisse Circulaire," *Les Comptes Rendus de l'Académie des Sciences de Paris, Série A*, Vol. 275, No. 10, Oct. 1972, pp. 667–670.
- [33] Laurence, J. C., "Intensity, Scale, and Spectra of Turbulence in Mixing Region of Free Subsonic Jet," NACA, Vol. 1292, 1957.
- [34] Liepmann, H. W., and Laufer, J., "Investigations of free turbulent mixing," NACA TN-1257, 1947.
- [35] Jordan, P., and Gervais, Y., "Modelling Self- and Shear-Noise Mechanisms in Inhomogeneous, Anisotropic Turbulence," *Journal of Sound and Vibration*, Vol. 279, Nos. 3–5, Jan. 2005, pp. 529–555. doi:10.1016/j.jsv.2003.11.045
- [36] Kovaszny, L. S. G., Kibens, V., and Blackwelder, R. F., "Large-Scale Motion in the Intermittent Region of a Turbulent Boundary Layer," *Journal of Fluid Mechanics*, Vol. 41, No. 2, 1970, pp. 283–325. doi:10.1017/S0022112070000629
- [37] Sabot, J., Renaud, J., and Comte-Bellot, G., "Space-Time Correlations of the Transverse Velocity Fluctuation in Pipe Flow," *Physics of Fluids*, Vol. 16, No. 9, 1973, pp. 1403–1405. doi:10.1063/1.1694532

R. Lucht
Associate Editor